THE JOURNAL OF PHYSICAL CHEMISTRY C

ARTICLE

pubs.acs.org/JPCC

Structure and Properties of Li−Si Alloys: A First-Principles Study

Hyunwoo Kim,[†,§] Chia-Yun Chou,[‡,§] John G. Ekerdt,[†] and Gyeong S. Hwang[*,†,‡]

[†]Department of Chemical Engineering, and [‡]Materials Science and Engineering Program, University of Texas at Austin, Austin, Texas 78712, United States

ABSTRACT: On the basis of density functional theory calculations, we present the energetics, structure, and electronic and mechanical properties of crystalline and amorphous Li−Si alloys. We also discuss the dynamic behavior of the alloys at finite temperatures based on ab initio molecular dynamics. When the Li content is sufficiently high, alloying between Li and Si is energetically favorable as evidenced by the negative mixing enthalpy; the alloy is most stable around 70 atom % Li in the crystalline phase and 70 ± 5 atom % Li in the amorphous phase. Our calculations unequivocally show that the incorporation of Li leads to disintegration of the tetrahedrally bonded Si network into small clusters of various shapes. Bader charge analysis shows that the charge state of Li remains nearly unchanged around +0.8, while that of Si varies approximately from −0.5 to −3.3 depending on the number of Si neighbors as can be understood as Zintl-like phases. Electronic structure analysis highlights that the charge transfer leads to weakening or breaking of Si−Si bonds with the growing splitting between 3s and 3p states, and consequently, the Li−Si alloys soften with increasing Li content.

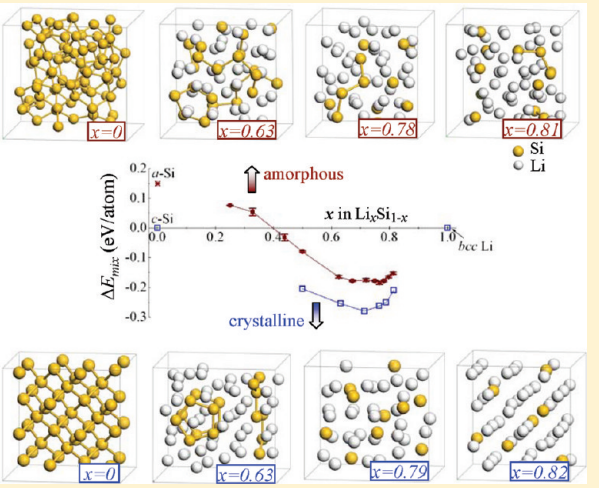

I. INTRODUCTION

Silicon-based materials have recently emerged as a promising candidate for anodes in lithium-ion batteries because they exhibit a higher energy-storage capacity than the conventional graphite anode. Silicon (Si) has a theoretical lithium (Li) capacity of $Li_{4.4}Si \approx 4200$ mAh/g, which is more than ten times greater than that of graphite (372 mAh/g)[1−3] Moreover, Si is safer, less expensive, and far more abundant than graphite. However, the practical use of Si as an anode material is hampered by its low intrinsic electrical conductivity and poor cycling performance.[4−7] In particular, the volume changes up to 400% during lithiation, and delithiation can cause severe cracking and pulverization of the Si electrode and consequent capacity fading arising from the loss of electrical contacts. Considerable efforts have been made to overcome these problems, for instance, through structural modifications such as amorphous phases,[8−10] nanoparticles,[11,12] nanowires,[13] and alloying with active/inactive elements such as silicon−tin[14] and silicon−metal[15−18] composites. In addition, first-principles calculations have recently been applied to investigate fundamental aspects of the structural changes and lithiation behavior of Si-based materials, but many of which still remain unclear.

Recent studies[19−24] have provided evidence for the formation of various stable lithium silicide crystalline phases such as $Li_{12}Si_7$, Li_7Si_3, $Li_{13}Si_4$, $Li_{15}Si_4$, and $Li_{22}Si_5$ during high-temperature lithiation. However, room-temperature Si lithiation frequently leads to amorphous lithium silicides (a−Li−Si).[25] It is therefore necessary to better understand the nature of amorphous Li−Si alloys, with comparisons to their crystalline counterparts. Very recently some theoretical efforts have been undertaken to understand the structure and properties of amorphous lithium silicides. Chevrier et al.[26,27] used a protocol in conjunction with density functional theory (DFT) to analyze the energetic and structural properties of disordered lithiated Si. Nonetheless, our understanding regarding the nature and properties of Li−Si alloys is still limited.

In this paper, we examine the energetics, structure, and electronic and mechanical properties of Li−Si alloys using DFT calculations. We first evaluate the relative stability of the alloys in both crystalline and amorphous phases by calculating their mixing enthalpies. Next, the structural evolution in terms of Li content and temperature is analyzed. Bader charge analysis is applied to estimate the charge states of Li and Si for various Li/Si composition ratios. While the Si network and electronic structure undergo considerable changes when alloyed with Li, the bulk modulus values for Li−Si alloys are calculated to assess the effect of increasing Li content on mechanical properties. In addition, ab initio molecular dynamics (AIMD) simulations are performed to look at the dynamic behavior of a few selected Li−Si alloys at finite temperatures.

Received: September 2, 2010
Revised: December 7, 2010
Published: January 12, 2011

Table 1. Calculated Lattice Constants and Corresponding Experimental Values (If Available) in Parentheses for Crystalline Li−Si Alloys Considered in This Work, Together with Crystallographic Description[a]

phases	space group	lattice constants (Å)	volume (Å^3)	# Li/Si	k-point mesh[b]	ref
Li	*Im*3(229)	a = 3.438 (3.436)	325.2	16/0	δ	28
Si	*Cm*(8)	a = 5.457 (5.430)	4387.6	0/216	α	29
LiSi	I41/a(88)	a = 9.353 (9.353), c = 5.753 (5.743)	31.5	8/8	χ	21,23
$Li_{12}Si_7$	*Pnma*(62)	a = 8.546 (8.600), b = 19.665 (19.755), c = 14.327(14.336)	43.0	96/56	β	24
Li_7Si_3	*C*2/*m*(12)	a = 4.3973,c = 17.928, γ = 120	50.0	40/16	χ	30
$Li_{13}Si_4$	*Pbam*(55)	a = 7.9195, b = 15.1057, c = 4.4423	66.4	26/8	χ	31
$Li_{15}Si_4$	$I\bar{4}3d$(220)	a = 10.623 (10.685)	74.9	60/16	χ	32
$Li_{22}Si_5$	*F*23(196)	a = 18.651	81.1	88/20	β	33

[a] For each structure, the number of Li and Si atoms (# Li/Si) per supercell and the k-point mesh size employed are also presented. [b] $\alpha = (2 \times 2 \times 2)$, $\beta = (3 \times 3 \times 3)$, $\chi = (5 \times 5 \times 5)$, $\delta = (11 \times 11 \times 11)$.

II. COMPUTATIONAL METHODS

The model structures of amorphous Li−Si alloys were created using AIMD simulations based on the atomic configurations of Au−Si alloys that were previously obtained using the combined modified embedded atom method (MEAM) and AIMD simulations (see ref 34 for detailed computational methods). According to the previous study,[34] Au and Si atoms in the bulk Au−Si amorphous alloy are overall well mixed with no segregation. The Au−Si interaction differs from the Li−Si interaction in nature, and thus the local atomic configurations (or short-range order) of the alloys tend to be dissimilar. Nonetheless, the Au−Si structure is likely a good starting configuration for the Li−Si amorphous structure (where Li and Si atoms are overall well dispersed as well); moreover, the high mobilities of Li and Si at high temperatures (>1000 K) allow facile local structure rearrangements to yield reliable Li−Si configurations within moderate annealing time. The Au atoms (in Au−Si alloys) were replaced by Li and Si atoms accordingly to achieve desired composition ratios; the replacement sites were carefully chosen such that Si and Li were well dispersed. The model structures, each containing 64 Li and Si atoms, were annealed at 1500 K for 2 ps with a time step of 1 fs and then rapidly quenched to 300 K at a rate of 0.6 K/fs, along with volume optimization. The annealing temperature was assured to be far above the alloy melting point (~1000 K) to accelerate the melting process and to eliminate any memory effects from the initial configuration. Here, the temperature was controlled via velocity rescaling. This approach can provide reasonable Li−Si amorphous structures at significantly reduced computational burden compared to starting with crystalline initial configurations. The crystalline Li−Si structures considered are summarized in Table 1.

The calculations reported herein were performed on the basis of density functional theory (DFT) within the generalized gradient approximation (GGA-PW91[35]), as implemented in the Vienna Ab-initio Simulation Package (VASP).[36−38] Spin polarization of the Li−Si system was also examined but appears to be insignificant. The projector augmented wave (PAW) method with a planewave basis set was employed to describe the interaction between ion cores and valence electrons. The PAW method is, in principle, an all-electron frozen-core approach that considers exact valence wave functions. Valence configurations employed are: $1s^2 2s^1$ for Li and $3s^2 3p^2$ for Si. An energy cutoff of 350 eV was applied for the planewave expansion of the electronic eigenfunctions. During geometry optimization, all atoms were fully relaxed using the conjugate gradient method until residual forces on constituent atoms become smaller than 5×10^{-2} eV/ Å. For Brillouin zone sampling, a $(2 \times 2 \times 2)$ k-point mesh in the scheme of Monkhorst−Pack[39] was used for all amorphous samples (each of which contains 64 atoms), sufficient considering the disordered structure: $(3 \times 3 \times 3) \sim (11 \times 11 \times 11)$ meshes for crystalline samples, depending on the sample size (see Table 1).

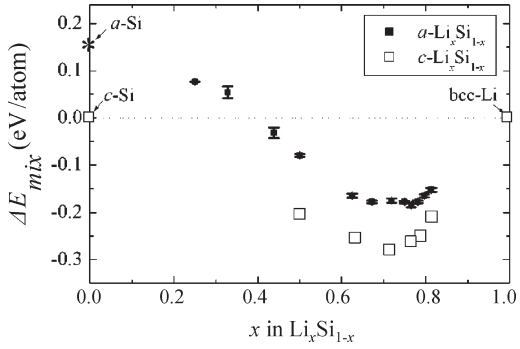

Figure 1. Variations in the mixing enthalpies of amorphous and crystalline Li−Si alloys as a function of Li content. The values for amorphous alloys are averaged based on five different 64-atom supercells.

III. RESULTS AND DISCUSSION

A. Structures and Stabilities. Figure 1 shows a variation in the mixing enthalpy for amorphous and crystalline Li−Si alloys as a function of Li:Si composition ratio, with respect to crystalline Si (c-Si) and body-centered cubic Li (bcc-Li). The mixing enthalpy per atom (ΔE_{mix}) is given by

$$\Delta E_{mix} = E_{Li_xSi_{1-x}} - xE_{Li} - (1-x)E_{Si}$$

where $E_{Li_xSi_{1-x}}$ is the total energy per atom of the Li−Si alloy examined; x is the atomic fraction of Li; and E_{Li} and E_{Si} are the total energies per atom of c-Si and bcc-Li, respectively.

For amorphous phases at low Li content, the mixing enthalpy is positive in value with respect to c-Si. As the Li content increases, this value drops and changes from positive to negative at 40 atom % Li. Above this Li content, the mixing enthalpy continues to decrease and falls to a valley plateau between 60 and 80 atom % Li. The positive value of mixing enthalpy at Li contents <40 atom % may indicate the presence of an initial barrier for Li incorporation into the crystalline Si matrix. Contrarily, the negative mixing enthalpy at Li contents >40 atom % suggests favorable alloy formation. According to the trend, amorphous

dx.doi.org/10.1021/jp1083899 |J. Phys. Chem. C 2011, 115, 2514–2521

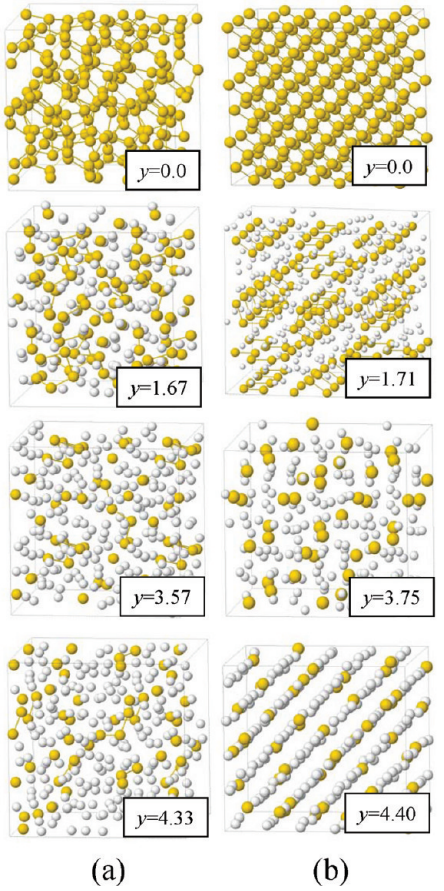

Figure 2. Atomic structures of (a) amorphous and (b) crystalline Li−Si alloys (Li_ySi where y indicates the Li content per Si). The yellow and white balls represent Si and Li atoms, respectively.

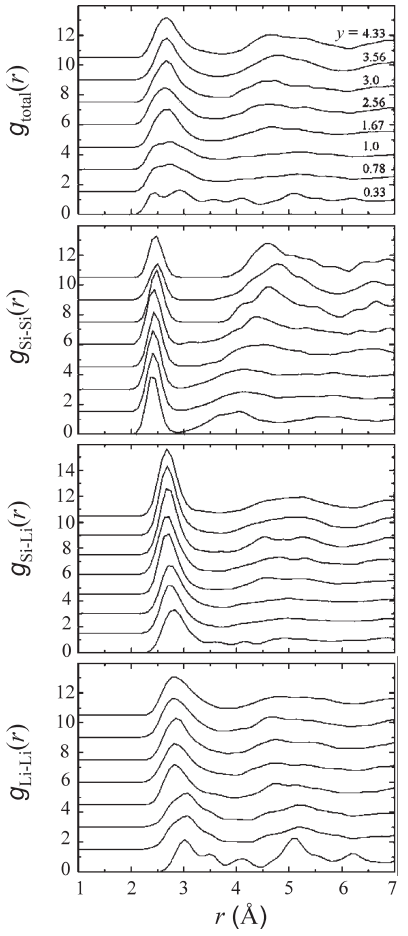

Figure 3. Total and partial pair-distribution functions for selected a-Li_ySi alloys; for each composition, five independent 64-atom samples were used to obtain good statistics.

Li−Si alloys with 60−80 atom % Li are most stable with an energy gain of 0.16−0.18 eV/atom with respect to c-Si and bcc-Li. Our calculations are consistent with previous experiments that evidenced the formation of a-$Li_{2.1}Si$ (≈ 68 atom % Li) with an energy gain of 0.12 eV.[25] For crystalline phases, a distinct mixing enthalpy minimum is found at 71 atom % Li, and on average the total energies are ∼0.1 eV/atom lower than their amorphous counterparts; hence, *a*−Li−Si alloys may undergo recrystallization at elevated temperatures, as evidenced by earlier experiments.[2]

We looked at the structural evolution of the amorphous Li_ySi alloy with varying Li contents from y = 0 to 4.4. Figure 2 shows a set of the amorphous structures from our simulations, together with corresponding crystalline structures for comparison. The amorphous structures were characterized using the pair distribution function (PDF, $g(r)$), which is defined as[40]

$$g(r) = \frac{V}{N}\frac{n(r)}{4\pi r^2 \Delta r}$$

where $n(r)$ represents particles in a shell within the region $r \pm \Delta r/2$, where Δr is the shell thickness and N denotes the number of particles in the model volume V.

Figure 3 shows the pair-distribution functions for selected amorphous Li_ySi alloys; for each composition, five independent 64-atom samples were used to obtain good statistics. No sharp second-neighbor peak is present, which confirms the amorphous nature (lack of long-range order) of the Li_ySi alloys. The total $g(r)$ of the $Li_{0.78}Si$ structure exhibits two distinct peaks at 2.4 and 2.7 Å, which are different from those of the remaining Li_ySi structures. The first peak originates from Si−Si pairs, whereas the second peak is attributed to a combination of Si−Li and Li−Li pairs. As the Li content increases, the second peak becomes stronger while the first peak dwindles. Furthermore, with increasing Li content, the Si−Si peak position shifts to larger pair distance, while the opposite trend is found for the Li−Li peak. This is indicative of the weakened Si−Si bonds; note that the charge transferred from Li fills up the antibonding sp^3 states of Si and thereby weakens the Si−Si bonds as discussed in ref 41.

Table 2 lists the calculated average and standard deviation values for the coordination number (CN) of Si in the selected alloys as a function of cutoff radius (r). At $r \leq 2.6$ Å, the average CN decreases from 3.34 to 2.33 with increasing y from 0.5 to 4.33, and an opposite trend is observed for $r \leq 3.1$ Å, where CN increases from 6.54 to 9.97. Considering the Si−Si bond length of ≈2.5 Å in a-Si and the Li−Si bond length of 2.57−3.09 Å in *c*-Li_ySi alloys, the CN at $r < 2.6$ Å represents the number of Si neighbors, and CN at $r \leq 3.1$ Å represents the number of Si and Li neighbors combined. The a-Si structure is composed of a sparse Si network, but as Li content increases, the Li−Si alloy becomes more densely packed as evident by the increasing CN. We also find that at r = 3.1 Å,the CN of Si is 10.04 in a-$Li_{3.57}Si$ and 9.97 in a-$Li_{4.33}Si$, indicating the former is more highly packed (albeit to a small degree). Note that the more densely packed

dx.doi.org/10.1021/jp1083899 |*J. Phys. Chem. C* 2011, 115, 2514–2521

Table 2. Average and Standard Deviation (In Parentheses) of the Calculated Average Coordination Number (CN) of Si in Selected Amorphous Li_ySi Alloys As a Function of Cut-off Radius (r in Å)

y	r = 2.5	r = 2.6	r = 2.7	r = 2.8	r = 2.9	r = 3.1
0.33	2.92 (0.01)	3.36 (0.02)	3.77 (0.02)	4.45 (0.02)	4.88 (0.02)	5.68 (0.01)
0.78	2.61 (0.21)	3.26 (0.15)	4.42 (0.05)	5.47 (0.13)	6.32 (0.09)	7.50 (0.22)
1.00	2.28 (0.17)	3.44 (0.05)	5.01 (0.02)	6.31 (0.18)	7.39 (0.16)	7.39 (0.16)
1.67	2.20 (0.07)	3.28 (0.14)	4.95 (0.04)	6.64 (0.12)	7.59 (0.30)	9.12 (0.29)
2.56	1.69 (0.29)	3.18 (0.38)	5.27 (0.21)	6.62 (0.44)	7.80 (0.55)	9.15 (0.69)
3.00	1.65 (0.22)	2.78 (0.05)	5.16 (0.01)	6.91 (0.06)	8.04 (0.28)	9.69 (0.22)
3.57	1.19 (0.06)	2.84 (0.26)	5.40 (0.27)	7.31 (0.38)	8.66 (0.35)	10.04 (0.37)
4.33	1.23 (0.33)	2.33 (0.30)	5.28 (0.07)	7.17 (0.44)	8.58 (0.22)	9.97 (0.29)

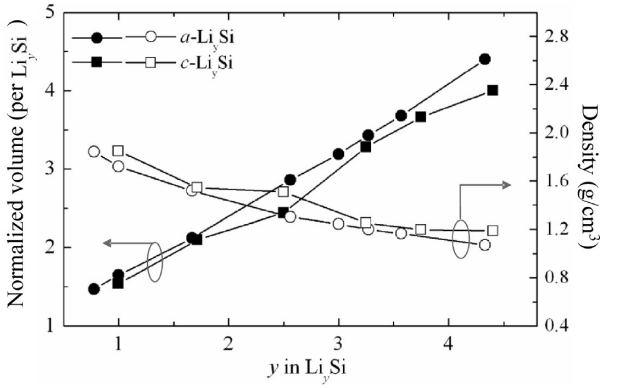

Figure 4. Variation in the volume and density of amorphous and crystalline Li−Si alloys as a function of Li content, as indicated. The volume (per Li_ySi) of each alloy is normalized with respect to that of c-Si.

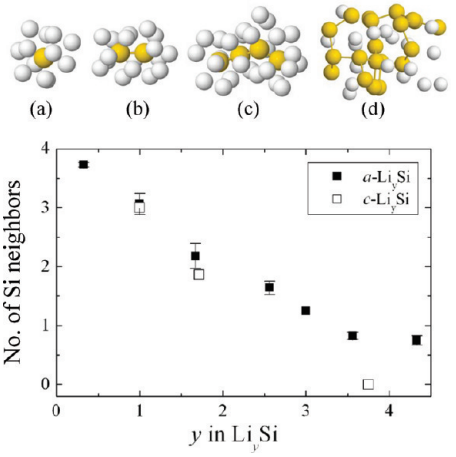

Figure 5. (Lower panel) Si−Si coordination number (CN) versus Li content (y) for various a-Li_ySi and c-Li_ySi alloys. (Upper panels) Representative Si clusters found in the amorphous alloys: (a) monomer, (b) dumbbell, (c) Si_4 string, (d) 3-fold coordinated Si network. The yellow and white balls represent Si and Li atoms, respectively.

a-$Li_{3.57}Si$ also has a slightly lower mixing enthalpy than a-$Li_{4.33}Si$, and the same relationship is found for their crystalline counterparts, suggesting energetically a-$Li_{3.57}Si$ might be more favorable than a-$Li_{4.33}Si$.

On the basis of the model structures, the variations in volume and density as a function of Li content were calculated as shown in Figure 4; the volume of each alloy is normalized with respect to that of c-Si (in which each Si occupies a volume of ≈20.47 Å^3). For both crystalline and amorphous phases, the volume increases nearly linearly with Li content, and the opposite trend is true for the density values. As expected, the crystalline phase is slightly denser than the amorphous alloy of corresponding composition. The fully lithiated a-$Li_{4.33}Si$ (c-$Li_{4.4}Si$) phase is predicted to yield a 334 (296) % volume expansion, which is in good agreement with ≈300% from previous experimental measurements.[17]

It was also found that the tetrahedrally bonded network of Si disintegrates into smaller Si fragments with increasing Li content. In crystalline phases, the diamond cubic structure of c-Si breaks up into small clusters in various shapes.[21,23,24] For instance, c-LiSi has a 3-fold-coordinated Si network that consists of interconnected chains and puckered eight-membered rings; c-$Li_{12}Si_7$ has two types of clusters, Si_5 rings and Si_4 stars; c-Li_7Si_3 has Si_2 dumbbells; c-$Li_{13}Si_4$ has a mixture of Si_2 dumbbells and Si atoms; and c-$Li_{15}Si_4$ and c-$Li_{22}Si_5$ have only single Si atoms. Likewise, in amorphous phases, the disintegration of a-Si into low-connectivity Si clusters also occurs as the Li content increases. Figure 5 (lower panel) shows the Si−Si coordination number versus Li content (y) for various a-Li_ySi and c-Li_ySi alloys, together with representative Si clusters found in the amorphous phases (upper panels). a-LiSi has Si_3 and Si_4 coordinated networks; a-$Li_{1.67}Si$ has mixed $Si_4 \sim Si_6$ strings and rings (as also reported in ref 42); a-$Li_{2.56}Si$ has Si_3 clusters, Si_2 dumbbells, and Si atoms; a-$Li_{3.57}Si$ has Si_3 and Si_4 strings; and a-$Li_{4.33}Si$ has Si_2 dumbbells and Si atoms. In amorphous phases, roughly 30−40% of Si atoms still form Si−Si pairs even in highly lithiated states (a-$Li_{3.57}Si$ and a-$Li_{4.33}Si$); however, in crystalline phases (c-$Li_{15}Si_4$ and c-$Li_{22}Si_5$), all Si atoms are isolated, as shown in Figure 5.

B. Dynamic Behaviors at Finite Temperatures. We performed ab initio molecular dynamics (AIMD) simulations in the canonical (NVT) ensemble to examine the dynamic behavior of Li and Si in $Li_{1.67}Si$ and $Li_{3.57}Si$ alloys. Three simulation temperatures were chosen: 300 K and 500 K in the amorphous state and 1050 K in the liquid state. For the amorphous cases, the alloy density was kept constant regardless of the temperature variation (see Figure 4 for the density values). In the liquid state, the experimental densities for Li−Si alloys of similar compositions and temperature were used (minor scaling was done as needed). For each alloy, the internal pressure as a function of cell volume was verified to ensure that the chosen density is reasonable. For the short-range order analysis, all three alloys examined were equilibrated at 300 and 500 K for 2 ps and at 1050 K for 6 ps; five different configurations were used for each alloy to produce averaged PDFs as shown in Figure 6. When the temperature increases, atoms spread around their average positions as the PDF peaks broaden and shrink in intensity. At 1050 K, the first peak is more broadened, but there is no significant deviation from the PDF profiles at 500 K;

dx.doi.org/10.1021/jp1083899 |J. Phys. Chem. C 2011, 115, 2514–2521

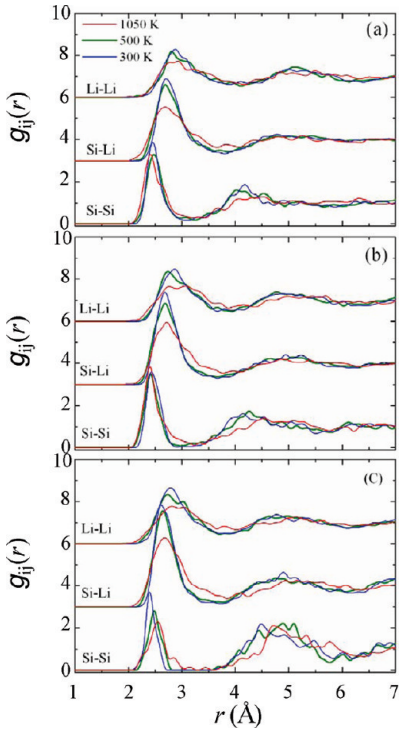

Figure 6. Pair distribution functions for (a) LiSi, (b) $Li_{1.67}Si$, and (c) $Li_{3.57}Si$ at 300 K (blue), 500 K (green), and 1050 K (red).

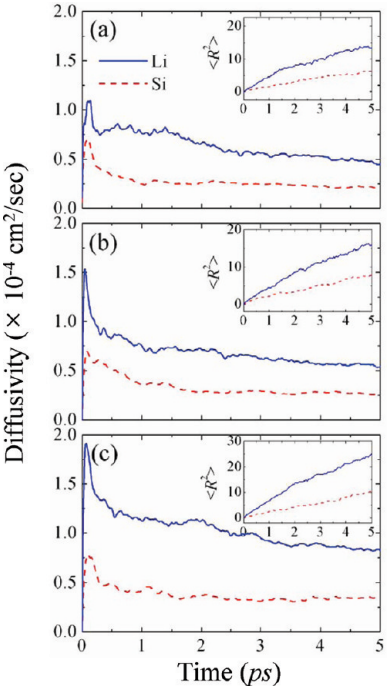

Figure 7. Variations in the diffusivities of Si (dotted) and Li (solid) in (a) LiSi, (b) $Li_{1.67}Si$, and (c) $Li_{3.57}Si$ at 1050 K as the simulation time progresses. The corresponding mean square displacements are also presented in the insets.

this may suggest the short-range order of Li−Si alloys is maintained even in the liquid state.

To better understand the dynamic properties, AIMD simulations were also performed to estimate Li and Si mobilities in molten LiSi, $Li_{1.67}Si$, and $Li_{3.57}Si$ alloys at 1050 K. The MD duration of 6 ps appears to be sufficient to obtain well-converged results, and for each alloy, five samples were averaged to calculate the mean-square displacements (MSD). Figure 7 shows the variations in MSD (insets) and diffusion constant of Si and Li as simulation time progresses. The MSDs are linearly proportional to time as can be expected from a liquid phase. The diffusion constants of Si and Li were calculated based on the Einstein relation

$$D = \frac{\langle |R_i(t) - R_i(0)|^2 \rangle}{6t}$$

where R_i is the atomic position; broken brackets denote thermal averages; and t is the time.

For LiSi, the diffusion coefficients were predicted to be $D_{Li} = 0.45 \pm 0.04 \times 10^{-4}$ and $D_{Si} = 0.20 \pm 0.05 \times 10^{-4}$ cm^2/s. For $Li_{1.67}Si$, $D_{Li} = 0.50 \pm 0.07 \times 10^{-4}$ and $D_{Si} = 0.23 \pm 0.07 \times 10^{-4}$ cm^2/s, which are comparable to the values reported in previous DFT calculations, $D_{Li} = 0.94 \times 10^{-4}$ and $D_{Si} = 0.42 \times 10^{-4}$ cm^2/s (within the simulation time of 2.8 ps).[42] For $Li_{3.57}Si$, the diffusivities increase to $D_{Li} = 0.73 \pm 0.06 \times 10^{-4}$ and $D_{Si} = 0.33 \pm 0.05 \times 10^{-4}$ cm^2/s. Note that despite the change in alloy composition the diffusion coefficient ratio between Li and Si remains more or less constant, $D_{Li}/D_{Si} \approx 2$. This is not surprising considering the mass dependence of diffusivity in a liquid-like phase, i.e., $D_2/D_1 \sim (m_1/m_2)^{1/2}$ for a disparate-mass binary mixture. Given that the atomic masses for Li and Si are 6.94 and 28.09 amu, respectively, our calculation result is consistent with what would be expected from the mass dependency, i.e., $D_{Li}/D_{Si} \approx (28.09/6.94)^{1/2} = 2.0$. Our calculations also show that Li mobility tends to be hindered by the heavier and slower Si atoms. At the highly lithiated case ($Li_{3.57}Si$), the diffusivity of Li is enhanced relative to that in LiSi or $Li_{1.67}Si$, while the diffusivity of Si also increases as facilitated by the fast diffusing Li.

Table 3. Calculated Charge States of Si and Li in c-Li−Si Alloys Based on the Grid-Based Bader Charge Analysis[a]

	LiSi	$Li_{12}Si_7$	Li_7Si_3	$Li_{15}Si_4$	$Li_{22}Si_5$
Si	−0.84	$-1.3^{(R)}$ $-0.46^{(SC)}$ $-1.88^{(ST)}$	$-2.05^{(D)}$	$-3.31^{(M)}$	$-3.31^{(M)}$
Li	+0.84	+0.84	+0.80 ~0.82	+0.80	+0.80 or $0(Li^0)$

[a] (R), ring; (SC), string center; (ST), string terminal; (D), dumbbell; (M), monomer.

For reference, the experimental self-diffusion coefficients for Li at 470 K and Si at 1687 K were reported to be $D_{Li} \approx 0.65 \times 10^{-4}$ cm^2/s[43] and $D_{Si} \approx 4.00 \times 10^{-4}$ cm^2/s.[44] Since there is no experimental data available, we approximated D_{Li} and D_{Si} at our simulation temperature of 1050 K using analytical models[45−50] that have been proposed to describe the temperature dependence of liquid diffusivity. Here, Si is assumed to be liquid at 1050 K for comparison purposes, although a-Si might start to melt above 1480 ± 50 K.[51] From these models, the Li and Si self-diffusion coefficients at 1050 K were roughly estimated to be 0.65−3.24 × 10^{-4} and 1.55−4.00 × 10^{-4} cm^2/s, respectively,[52] greater than the predicted values in the Li−Si alloys. The lower diffusivities might be attributed to the interaction between Li and Si; this is not surprising considering that the alloys are more stable than

dx.doi.org/10.1021/jp1083899 |J. Phys. Chem. C 2011, 115, 2514–2521

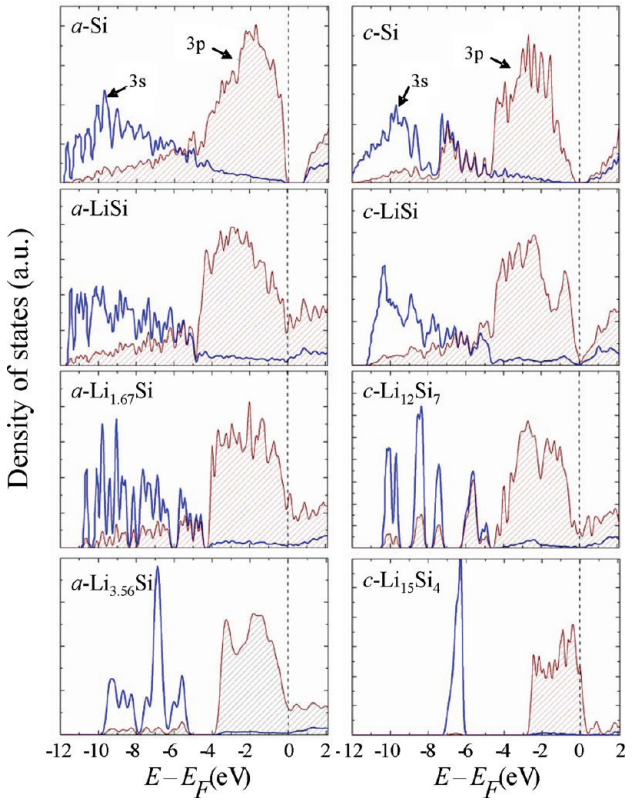

Figure 8. Electron density of states (DOS) projected on Si atoms in various Li−Si alloys, together with the DOS of pure Si for comparison. The vertical dotted line indicates the Fermi level position.

their pure counterparts as evidenced by the negative mixing enthalpy values presented earlier.

C. Electronic and Mechanical Properties. We calculated the charge states of Si and Li in c-Li$_y$Si and a-Li$_y$Si using the grid-based Bader analysis;[53] special care was taken to ensure convergence with respect to the grid size. As summarized in Table 3, the Si charge state significantly varies from −0.84 to −3.31 with increasing Li content from y = 1 to 4.4 in c-Li$_y$Si, while the Li charge state remains nearly unchanged (+0.8 ∼ +0.82). For highly lithiated amorphous phases (a-Li$_{3.57}$Si and a-Li$_{4.33}$Si) where Si_2 dimers and single Si atoms are prevailing, the charge states of Si and Li are estimated to be −2.38 (±0.41) for Si_2 dimers, −3.61 (±0.23) for Si monomers, and +0.8 (±0.02) for Li. The charge states of Si can be explained by general Zintl rules[54] with the consideration that only partial charge is transferred from Li to Si. For instance, the calculated charge states of Si dimers (in c-Li$_7$Si$_3$) and monomers (in c-Li$_{22}$Si$_5$) are −2.05 and −3.31, while if they were in perfect Zintl phases (transfer completes the octet shell of Si), these values should be close to −3.0 and −4.0, respectively.

Figure 8 shows the electron density of states (DOS) projected on Si atoms in selected amorphous and crystalline Li−Si alloys, along with the DOS of pure Si for comparison; the analysis could demonstrate how the Si−Si bonding property changes as a function of Li content. The Fermi level is used as a reference energy, which is set to be zero. As expected, pure Si exhibits strong s−p hybridization leading to the tetrahedral sp^3 structure, while the amorphous phase yields a larger band gap than the crystalline phase. As Li content increases, the degree of s−p hybridization decreases; note that the splitting between 3s and 3p states grows

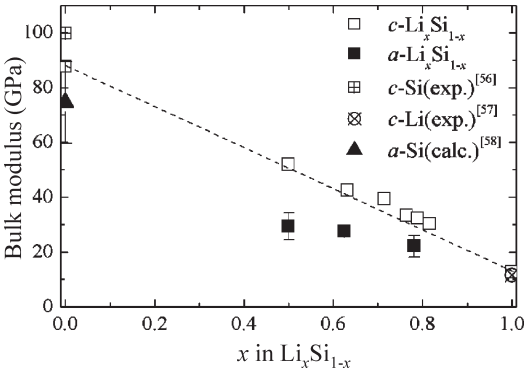

Figure 9. Bulk moduli for c-Li−Si and a-Li−Si alloys; the dotted line connecting c-Si and bcc-Li represents a linear relation between bulk modulus and x.

larger going from LiSi to their higher lithiated states. As the Li content increases, the Li−Si alloy bandgap gradually diminishes, showing more metallic character. In addition, the distributions of the 3s and 3p states get narrower with increasing Li content, which is apparently attributed to the decreasing Si−Si bonding interaction, as the Si network loses its connectivity and disintegrates into smaller fragments, as discussed earlier. We can also notice that the DOS profiles for the crystalline and amorphous phases have slightly different patterns at any given composition, which is mainly due to variations in the Si cluster shape (such as pairs, strings, rings, etc). For instance, a-Li$_{1.67}$Si has broader peaks than its crystalline counterpart (c-Li$_{12}$Si$_7$) because Si_3 ∼ Si_4 strings and rings in the former phase allow stronger Si−Si interaction than the Si_4 stars and Si_5 rings in the latter phase. Likewise, a-Li$_{3.57}$Si that also consists of a fair amount of Si_2 dimers has broader peaks than c-Li$_{15}$Si$_4$ containing only Si monomers.

Our calculations clearly demonstrate the gradual structural transformation as well as the softening of Si−Si bond strength as the Li content increases. Finally, we looked at how the changes in the atomic and electronic structures affect the mechanical properties of Li−Si alloys. Here, we only calculated the bulk modulus (B) for each alloy, which can be determined by fitting the Murnaghan equation of state[55] to the corresponding energy versus volume curve. In our calculations, uniform tensile and compressive stresses were imposed on the alloys to achieve ±10% volume variation.

$$E(V) = E_0 + \left(\frac{BV}{B'}\right)\left[\frac{(V_0/V)^{B'}}{B'-1}+1\right] - \frac{V_0 B}{(B'-1)}$$

where E and E_0 refer to the total energies of a given LiSi supercell at volume V and V_0 (equilibrium), respectively; B is the bulk modulus; and B' is the pressure derivative of the bulk modulus.

Figure 9 shows the variation in bulk moduli for c-Li−Si and a-Li−Si alloys. The calculated bulk modulus values for c-Si and bcc-Li are $B_{c\text{-}Si}$ = 87.8 GPa and $B_{bcc\text{-}Li}$ = 12.7 GPa, in good agreement with the experimental values of $B_{c\text{-}Si}$ = 100.0 GPa[56] and $B_{bcc\text{-}Li}$ = 11.6 GPa.[57] The dotted line connecting the bulk moduli of c-Si and bcc-Li represents a linear relation between the bulk modulus and the Li concentration (x). For both amorphous and crystalline Li−Si alloys, the bulk moduli indeed decrease with increasing Li content in a nearly linear manner leading to significant elastic softening. For a given Li content, the amorphous phase tends to be softer than its crystalline counterpart.

dx.doi.org/10.1021/jp1083899 |J. Phys. Chem. C 2011, 115, 2514–2521

IV. SUMMARY

We performed DFT-GGA calculations to examine the structure, stability, and properties of Li−Si alloys. According to the calculation results, the formation of the most stable structure tends to occur around 70 (70 ± 5) atom % Li for the crystalline (amorphous) phase with an energy gain of 0.27 (0.18) eV per atom with respect to c-Si and bcc-Li. For highly lithiated states (60−80 atom % Li), the crystalline structures are ≈0.1 eV more favorable than their amorphous counterparts. The volume of the Li−Si alloy increases nearly linearly with Li content, while the crystalline structure is slightly denser than the amorphous structure of corresponding composition; the fully lithiated a-$Li_{4.33}Si$ (c-$Li_{4.4}Si$) phase is predicted to yield a 334 (296) % volume expansion with respect to c-Si. Our calculations also demonstrate that with increasing Li content the tetrahedrally bonded Si network is weakened and subsequently undergoes disintegration into low-connectivity clusters of various shapes, including a three-coordinated Si network with interconnected chains and puckered eight-membered rings (c-LiSi), Si_5 rings and Si_4 stars (c-$Li_{12}Si_7$), Si_2 dumbbells and Si atoms (c-$Li_{13}Si_4$), and only single Si atoms (c-$Li_{15}Si_4$ and c-$Li_{22}Si_5$). Unlike the crystalline case, roughly 30−40% of Si atoms tend to remain in Si−Si pairs even in highly lithiated amorphous phases (a-$Li_{3.57}Si$ and a-$Li_{4.33}Si$). A series of AIMD simulations show that the short-range order of Li−Si alloys tends to be maintained even in the molten state, while the Li−Si interaction likely leads to a drop in Li and Si diffusivities when alloyed with each other. According to Bader charge analysis, while the Li charge state remains nearly unchanged around +0.80 to +0.82, the Si charge state varies significantly from −0.46 to −3.31 depending on the number of Si neighbors as can be understood with Zintl electron counting rules. Our electron DOS analysis also demonstrates that toward higher lithiated states the Si s−p splitting grows larger accompanied by weakening/breaking of Si−Si bonds and changes in the alloy structure. The Li−Si alloy bandgap gradually diminishes with increasing Li content, showing more metallic character. The bulk modulus of the Li−Si alloy is predicted to decrease almost linearly with increasing Li content, due to the structural transformation as well as the softening of Si−Si bond strength. The fundamental findings assist in understanding the nature of Li−Si alloys further, and the present work can also provide a framework for the study of various lithiated alloys.

AUTHOR INFORMATION

Corresponding Author

*E-mail: gshwang@che.utexas.edu.

Author Contributions

§These authors equally contributed to this work

ACKNOWLEDGMENT

GSH greatly acknowledges the Robert A. Welch Foundation (F-1535) for partial support of this work. We would like to thank the Texas Advanced Computing Center for use of their computing resources.

REFERENCES

(1) Winter, M.; Besenhard, J. O. *Electrochim. Acta* **1999**, *45*, 31.
(2) Sharma, R. A.; Seefurth, R. N. *J. Electrochem. Soc.* **1976**, *123*, 1763.
(3) Boukamp, B. A.; Lesh, G. C.; Huggins, R. A. *J. Electrochem. Soc.* **1981**, *128*, 725.
(4) Beaulieu, L. Y.; Eberman, K. W.; Turner, R. L.; Krause, L. J.; Dahn, J. R. *Electrochem. Solid-State Lett.* **2001**, *4*, A137.
(5) Ryu, J. H.; Kim, J. W.; Sung, Y. E.; Oh, S. M. *Electrochem. Solid-State Lett.* **2004**, *7*, A306.
(6) Obrovac, M. N.; Christensen, L. *Electrochem. Solid-State Lett.* **2004**, *7*, A93.
(7) Maranchi, J. P.; Hepp, A. F.; Kumta, P. N. *Electrochem. Solid-State Lett.* **2003**, *6*, A198.
(8) Netz, A.; Huggins, R. A.; Weppner, W. *J. Power Sources* **2003**, *119−121*, 95.
(9) Bourderau, S.; Brousse, T.; Schleich, D. M. *J. Power Sources* **1999**, *81−82*, 233.
(10) Hatchard, T. D.; Dahn, J. R. *J. Electrochem. Soc.* **2004**, *151*, A838.
(11) Gao, B.; Sinha, S.; Fleming, L.; Zhou, O. *Adv. Mater.* **2001**, *13*, 816.
(12) Graetz, J.; Ahn, C. C.; Yazami, R.; Fultz, B. *Electrochem. Solid-State Lett.* **2003**, *6*, A194.
(13) Chan, C. K.; Peng, H.; Liu, G.; McIlwrath, K.; Zhang, X. F.; Huggins, R. A.; Cui, Y. *Nat. Nanotechnol.* **2008**, *3*, 31.
(14) Beaulieu, L. Y.; Hewitt, K. C.; Turner, R. L.; Bonakdarpour, A.; Abdo, A. A.; Christensen, L.; Eberman, K. W.; Krause, L. J.; Dahn, J. R. *J. Electrochem. Soc.* **2003**, *150*, A149.
(15) Mao, O.; Turner, R. L.; Courtney, I. A.; Fredericksen, B. D.; Buckett, M. I.; Krause, L. J.; Dahn, J. R. *Electrochem. Solid-State Lett.* **1999**, *2*, 3.
(16) Fleischauer, M. D.; Topple, J. M.; Dahn, J. R. *Electrochem. Solid-State Lett.* **2005**, *8*, A137.
(17) Beaulieu, L. Y.; Hatchard, T. D.; Bonakdarpour, A.; Fleischauer, M. D.; Dahn, J. R. *J. Electrochem. Soc.* **2003**, *150*, A1457.
(18) (a) Nazri, G. A.; Pistoia, G. *Lithium Batteries Science and Technology*; Kluwer Academic Plenum: Boston, 2004. (b) Anani, A.; Crouch-Baker, S.; Huggins, R. A. *J. Electrochem. Soc.* **1987**, *134*, 3098.
(19) Anantharaman, T. R. *Metallic glasses: production properties and applications*; Aedermannsdorf, Switzerland: Trans Tech Publications, 1984.
(20) Massalski, T. B. In *Binary Alloys Phase Diagram*; Massalski, T. B., Ed.; ASM International: Materials Park, OH, 1990; p 2465.
(21) Stearns, L. A.; Gryko, J.; Diefenbacher, J.; Ramachandran, G. K.; McMillan, P. F. *J. Solid State Chem.* **2003**, *173*, 251.
(22) Kubota, Y.; Escano, M. C. S.; Nakanishi, H.; Kasai, H. *J. Appl. Phys.* **2007**, *102*, 053704.
(23) Kubota, Y.; Escano, M. C. S.; Nakanishi, H.; Kasai, H. *J. Alloys Compd.* **2008**, *458*, 151.
(24) van Leuken, H.; de Wijs, G. A.; van der Lugt, W.; de Groot, R. A. *Phys. Rev. B* **1996**, *53*, 10599.
(25) Limthongkul, P.; Jang, Y. I.; Dudney, N. J.; Chiang, Y. M. *Acta Mater.* **2003**, *51*, 1103.
(26) Chevrier, V. L.; Dahn, J. R. *J. Electrochem. Soc.* **2009**, *156* (6), A454–A458.
(27) Chevrier, V. L.; Dahn, J. R. *J. Electrochem. Soc.* **2010**, *157* (4), A392–A398.
(28) Smith, H. G.; Berliner, R.; Jorgensen, J. D.; Nielsen, M.; Trivisonno, J. *Phys. Rev. B* **1990**, *41*, 1231.
(29) Ashcroft, N. W.; Mermin, N. D. *Solid State Physics*; Harcourt: Orlando, 1976.
(30) Bohm, M. C.; Ramirez, R.; Nesper, R.; von Schnering, H. G. *Phys. Rev. B* **1984**, *30*, 4870.
(31) von Schnering, H. G.; Nesper, R.; Curda, J.; Tebbe, K. F.; Curda, J. *Z. Metallkd.* **1980**, *71*, 357.
(32) Frank, U.; Muller, W.; Schafer, H. *Z. Naturforsch.* **1975**, *30*, 10.
(33) Nesper, R.; Schnering, H. G.von *J. Solid State Chem.* **1987**, *70*, 48.
(34) Lee, S.-H.; Hwang, G. S. *J. Chem. Phys.* **2007**, *127*, 224710.
(35) Blochl, P. E. *Phys. Rev. B* **1994**, *50*, 17953.
(36) Kresse, G.; Hafner, J. *Phys. Rev. B* **1993**, *47*, 558.

(37) Kresse, G.; Furthmuller, J. *Comput. Mater. Sci.* **1996**, *6*, 15.
(38) Kresse, G.; Furthmuller, J. *Phys. Rev. B* **1996**, *54*, 11169.
(39) Monkhorst, H. J.; Pack, J. D. *Phys. Rev. B* **1976**, *13*, 5188. Rahman, A. *Phys. Rev.* **1964**, *146*, A405.
(40) Allen, M.; Tildesley, D. *Computer simulation of liquids*; Oxford University Press: New York, 1987; p 54.
(41) Kim, H.; Kweon, K. E; Chou, C. Y.; Ekerdt, J. G.; Hwang, G. S. *J. Phys. Chem. C* **2010**, *114*, 17942.
(42) de Wijs, G. A.; Pastore, G.; Selloni, A.; van der Lugt, W. *Phys. Rev. B* **1993**, *48*, 13459.
(43) Murday, J. S.; Cotts, R. M. *Z. Naturforsch.* **1971**, *A 26*, 85.
(44) Sanders, P. G.; Aziz, M. J. *J. Appl. Phys.* **1999**, *86*, 4258.
(45) Yang, S.; Su, X.; Wang, J.; Yin, F.; Tang, N. *Metall. Mater. Trans. A* **2009**, *40A*, 3108.
(46) Cohen, M. H.; Turnbull, D. *J. Chem. Phys.* **1959**, *31*, 1164.
(47) Ercolessi, F.; Tosatti, E.; Parrinello, M. *Phys. Rev. Lett.* **1986**, *57*, 719–22.
(48) Lopez, M. J.; Jellinek, J. *Phys. Rev. A* **1994**, *50*, 1445–58.
(49) Liu, C. S.; Xia, J.; Zhu, Z. G.; Sun, D. Y. *J. Chem. Phys.* **2001**, *114*, 7506–12.
(50) Willaime, F.; Massobrio, C. *Phys. Rev. Lett.* **1989**, *63*, 2244–47.
(51) Thompson, M. O.; Galvin, G. J.; Mayer, J. W.; et al. *Phys. Rev. Lett.* **1984**, *52*, 2360–63.
(52) The activated state model,[47] $D \sim \exp(-1/T)$; moving oscillator model,[48] $D \sim T$; density fluctuation model,[49] $D \sim T^2$; free volume model,[50] $D \sim T^{1/2} \exp(-1/T)$. From these models, the Li (Si) self-diffusion coefficients at 1050 K were estimated to be $0.65(4.00) \times 10^{-4}$, $1.45(2.49) \times 10^{-4}$, $3.24(1.55) \times 10^{-4}$, and $0.97(3.15) \times 10^{-4}$ cm^2/s, respectively.
(53) Henkelman, G.; Arnaldsson, A.; Jonsson, H. *Comput. Mater. Sci.* **2006**, *36*, 354.
(54) Kauzlarich, S. M. *Chemistry, Structure, and Bonding of Zintl Phases and Ions*; Wiley-VCH Publishers: New York, 1996.
(55) Murnaghan, F. D. *Proc. Natl. Acad. Sci.* **1944**, *30*, 244–247.
(56) Asher, J.; Jones, O. C.; Noyes, J. G.; Phillips, G. F. Eds. *Kaye & Laby's Tables of Physical and Chemical Constants*, 16th ed.; Longman: Harlow, Essex, 1995; Vol. 45, p 214.
(57) Simmons, G.; Wang, H. *Single Crystal Elastic Constants and Calculated Aggregate Properties: A Handbook*; MIT press: Cambridge, MA, 1971.
(58) Bondi, R. J.; Lee, S.; Hwang, G. S. *Phys. Rev. B* **2010**, *81*, 195207.